Lab on a Chip

Rapid Parallel Generation of a Fluorescently Barcoded Drop Library from a Microtiter Plate Using the Plate-Interfacing Parallel Encapsulation (PIPE) Chip

SCHOLARONE™
Manuscripts

Rapid Parallel Generation of a Fluorescently Barcoded Drop Library from a Microtiter Plate Using the Plate-Interfacing Parallel Encapsulation (PIPE) Chip†

Geoffrey K. Zath[1,2]‡, Ralph A. Sperling[4,5]‡, Carter W. Hoffman[1,2], Dimitri A. Bikos[1,2], Reha Abbasi[1,2], Adam R. Abate[5], David A. Weitz[4,7], Connie B. Chang[1,2,3]*

[1]Center for Biofilm Engineering, Montana State University, Bozeman, MT, USA

[2]Department of Chemical and Biological Engineering, Montana State University, Bozeman, MT, USA

[3]Department of Physiology and Biomedical Engineering, Mayo Clinic, Rochester, MN, USA

[4]Department of Physics, School of Engineering and Applied Sciences, Harvard University, Cambridge, MA, USA

[5]Fraunhofer Institute for Microengineering and Microsystems IMM, Mainz, Germany

[6]Department of Bioengineering and Therapeutic Sciences, University of California, San Francisco, CA, USA

[7]Wyss Institute for Biologically Inspired Engineering at Harvard University, Boston, MA, USA

‡ Authors contributed equally

*To whom correspondence may be addressed: Connie B. Chang, Department of Physiology and Biomedical Engineering, Mayo Clinic, 200 1st St SW, Rochester, MN 55902, conniebchang@gmail.com

Abstract

In drop-based microfluidics, an aqueous sample is partitioned into drops using individual pump sources that drive water and oil into a drop-making device. Parallelization of drop-making devices is necessary to achieve high-throughput screening of multiple experimental conditions, especially in time-sensitive studies. Here, we present the Plate-Interfacing Parallel Encapsulation (PIPE) chip, a microfluidic chip designed to generate 50- to 90-μm diameter drops of up to 96 different conditions in parallel by interfacing individual drop makers with a standard 384-well microtiter plate. The PIPE chip is used to generate two types of optically barcoded drop libraries consisting of two-color fluorescent particle combinations: a library of 24 microbead barcodes and a library of 192 quantum dot barcodes. Barcoded combinations in the drop libraries are rapidly measured within a microfluidic device using fluorescence detection and distinct barcoded populations in the fluorescence drop data are identified using DBSCAN data clustering. Signal analysis reveals that particle size defines the source of dominant noise present in the fluorescence intensity distributions of the barcoded drop populations, arising from Poisson loading for microbeads and shot noise for quantum dots. A barcoded population from a drop library is isolated using fluorescence-activated drop sorting, enabling downstream analysis of drop contents. The PIPE chip can improve multiplexed high-throughput assays by enabling simultaneous encapsulation of barcoded samples stored in a well plate and reducing sample preparation time.

Introduction

48

49   Drop-based microfluidics technology reduces assay times and increases sample throughput

50 by rapidly creating and analyzing picoliter-sized drops.[1, 2] Drop-based microfluidics has recently

51 been applied towards combinatorial drug discovery,[3] massively multiplexed nucleic acid

52 detection,[4] and antibiotic susceptibility screening.[5] In these assays, 10^3 to 10^6 drops are tracked by

53 a unique identifier in each drop, called a "barcode". This is commonly achieved using one of two

54 barcode types: DNA barcodes introduced to tag drop contents as part of a next generation

55 sequencing pipeline;[6-9] or fluorescent dyes and particles used to label drops for fluorescence-based

56 assays, such as enzyme activity or dose-response screening.[3-5, 10-14] DNA barcoding can provide

57 upwards of 10^7 unique identifiers, enabling large-scale single-cell transcriptomics, but requires

58 coalescing the drop emulsion before sequencing.[6-9] Though an advantage in single cell sequencing,

59 drop coalescence prohibits ultrahigh-throughput experiments in which drop contents are assayed

60 over time. Fluorescent labeling allows the barcode and fluorescent assay output to be measured

61 simultaneously without coalescing the drops. The resulting collections of either DNA or

62 fluorescent barcodes in drops, known as "libraries", enable multiplexed or combinatorial readouts

63 of the unique components encapsulated within the drops.[10-13]

64   A typical method for creating a barcode within a drop library is to emulsify a fixed sample

65 volume of that barcode contained within a microtiter plate well or microcentrifuge tube using a

66 single drop-making device. The process rapidly becomes labor- and time-intensive when a single

67 drop-making device is used to generate increasingly large numbers of barcoded drops that are

68 subsequently pooled together. Individual microfluidic drop makers can be run in parallel, but this

69 requires multiple pump sources to emulsify each sample. Alternatively, liquid handling machines

70 or autosamplers can be programmed to sequentially load individual samples from a microtiter plate

71 into a microfluidic device;[14-17] however, these technologies are costly and cannot create multiple

72 different barcodes simultaneously, which may be necessary for time-sensitive experiments. For

73 example, all samples must be emulsified and processed in parallel to accurately capture the time-

74 sensitive kinetics needed for performing comparative rapid enzymatic reaction screening studies.[18,

75 19] Thus, to perform parallel encapsulation of multiple different barcodes, specialized microfluidic

76 devices actuated using vacuum[20] or positive pressure[7, 8] and containing multiple drop makers have

77 been designed to interface with wells on standard microtiter plates. Prior work from Rotem *et al.*

78 used such a device to encapsulate DNA barcodes to perform single-cell chromatin profiling.[7, 8]

79 However, the fabrication of this device was not described in detail, nor was the device used to

80 create fluorescently barcoded libraries. Extending the utility of this device for fluorescent

81 barcoding would enable multiplexed assaying, wherein a barcoded signal is simultaneously

82 measured along with an assay output. Additionally, fluorescently barcoded drops enable sample

83 isolation and enrichment of a particular sample using fluorescence-activated drop sorting.[21, 22] To

84 allow for longer term storage of the drop libraries, fluorescent particles may be used in the place

85 of dyes[3, 11] to prevent diffusion of barcode labels between drops.[23]

86 Here, we detail the fabrication of a microfluidic device comprised of 96 simultaneously

87 operating drop makers called the Plate-Interfacing Parallel Encapsulation (PIPE) chip that directly

88 interfaces with 96 wells of a standard 384-well microtiter plate. The PIPE chip is operated within

89 a pressure chamber, a modified commercial pressure cooker, wherein pressurized air drives

90 parallelized drop formation across the 96 drop makers on the device. Parallelization enables rapid

91 creation of drop libraries at a total drop throughput of approximately 300 kHz, approximately two

92 orders of magnitude larger than serial drop generation using a single drop-making device, creating

93 a total of approximately 3.6×10^7 drops in 2 min. Drop sizes produced by the PIPE chip are

94   described using a simple drop scaling law, which allows for fine-tuning of drop diameters ranging

95   from approximately 50 - 90 μm. The PIPE chip is used to create two types of optically barcoded

96   drop libraries using two-color combinations of either microbeads or quantum dots (QDs). A

97   quarter of the 96 drop makers on the PIPE chip was used to create a drop library consisting of 24

98   fluorescent microbead combinations. The PIPE chip was also used twice to create a drop library

99   consisting of 192 QD combinations. Fluorescence from each barcoded drop was measured at high

100   speed using a flow-based detection method[22] to create a two-color scatter plot for each type of

101   barcode library. A data clustering method, density-based spatial clustering of applications with

102   noise (DBSCAN),[24] is used to identify uniquely barcoded concentrations and minimize the signal

103   overlap between the combinations. The dominant sources of noise influencing the fluorescence

104   signal overlap between barcode populations arise from Poisson loading for drops containing

105   fluorescent microbeads approximately 1 μm in diameter and shot noise of the photodetector for

106   drops containing QDs approximately 10 nm in diameter. The effect of these noise sources when

107   designing barcode label concentration can be accounted for by scaling the barcode particle

108   concentration with a quadratic function, thereby allowing for quick prototyping of barcode library

109   labels. Finally, we demonstrate the utility of the PIPE chip by sorting and isolating a single

110   fluorescently barcoded sample from a drop library of 24 different barcode combinations.[21, 22] The

111   ability to sort a specific barcoded sample from a drop library enables further analysis of drop

112   contents using downstream techniques such as PCR amplification and genetic sequencing.[25-27]

113   Drop libraries created with the PIPE chip can help to streamline existing multiplexed assays, such

114   as combinatorial drug screening[3] or high-throughput assaying of protease activity,[12] by enabling

115   simultaneous encapsulation of barcoded samples stored in a well plate.

116

117

Materials and Methods
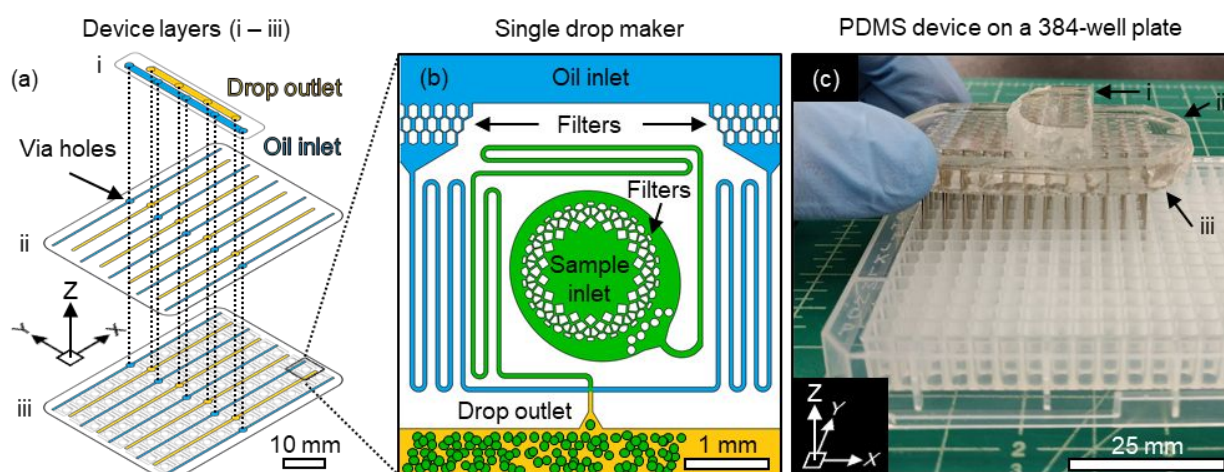
119 **PIPE Chip Design**

120   The PIPE chip was fabricated from three separate approximately 5-mm thick layers of

121 polydimethylsiloxane (PDMS) plasma bonded on top of one another to form a 3-dimensional

122 network of channels. The top layer of the device (Fig. 1a, i) is comprised of a narrow strip of

123 PDMS containing two long channels that function as a common oil inlet and drop outlet for all

124 three layers. Oil inlet and drop outlet channels run perpendicular to the channels in the remaining

125 two PDMS layers, thereby allowing oil and drops to flow throughout the device from a single inlet

126 and outlet, respectively. The oil inlet channel (Fig. 1a, i, blue) and drop outlet channel (Fig. 1a, i,

127 yellow) are connected to the rest of the device through a total of nine via holes punched in the

128 middle layer (Fig. 1a, ii), five for oil distribution and four for drop collection, providing a pathway

129 for fluids from the top layer through to the bottom layer (Fig. 1a, dashed black lines). The middle

130 layer contains oil distribution and drop collection channels that pass the oil phase to the drop

131 makers and collect produced drops. The bottom layer (Fig. 1a, iii) contains 96 drop makers (Fig.

132 1b), each connected to oil distribution and drop collection channels. Drop maker inlet holes are

133 spaced 4.5 mm apart to match the standard pitch of a 384-well microtiter plate, enabling the PIPE

134 chip to interface directly to ¼ of a 384-well microtiter plate.

135

136 **PIPE Chip Fabrication**

137   Each of the PDMS layers i – iii (Fig. 1a) was cast from a unique master mold and bonded

138 following standard techniques in soft lithography (see ESI *PIPE Chip Fabrication* for details).†[22]

139 Short lengths (22.5 mm) of SAE 304 stainless steel capillary tubes (0.71 mm OD, 0.41 mm ID,

140   Vita Needle) were fitted into the sample inlet holes of the device to provide a path for fluids from

141   each microtiter plate well to the sample inlet of each drop maker (Fig. 1b). For encapsulating

142   barcoded samples, the device was manually positioned above ¼ of a standard 384-well microtiter

143   plate such that each of the stainless steel inlet capillaries nearly extended to the bottom of a

144   different well (Fig. 1c).

145
146   **Fig. 1** PIPE chip design and assembly. (a) The PIPE chip was assembled from three layers: (i) a
147   top layer containing oil distribution (blue) and drop collection (yellow) channels connected to a
148   single inlet and outlet, respectively; (ii) a middle layer which reduces fluidic resistance by
149   providing additional height to the oil and drop collection distribution channels on the bottom layer;
150   and (iii) a bottom layer which contains an array of 96 drop makers (eight rows of twelve drop
151   makers) with channels for oil distribution (five rows, blue) and drop collection (four rows, yellow).
152   (b) Detailed view of one of the 96 drop makers positioned on the bottom layer. Colors are used to
153   distinguish oil inlet (blue), aqueous sample inlet (green), and drop outlet (yellow) channels. (c)
154   Image of a completed device interfaced with ¼ of a 384-well plate. Each layer (i – iii) of the fully
155   assembled device from part (a) is indicated using black arrows. Stainless steel sample inlet
156   capillary tubes are visible extending into the microtiter plate wells below.
157

158   **Pressure Chamber**

159   The barcoded samples contained in the wells of the microtiter plate were simultaneously

160   driven into each of the 96 drop makers of the PIPE chip under the uniform pressure within the

161   sealed aluminum interior chamber of a 6-quart pressure cooker (Fig. 2a). Compressed air

162   (approximately 60 psig) supplied both the oil reservoir pressure P_{oil} and chamber pressure P_{water},

163   both adjusted from 0-15 psig using manual regulators (McMaster-Carr 6745K32 0-25 psi) and

164   analog gauges (McMaster-Carr 3850K2 0-15 psi). The oil reservoir was comprised of a pressure-

165   rated glass bottle (Sigma Duran Z674397) and a cap fitted with ports for compressed air and oil

166   inlet tubing. Custom-drilled ports in the pressure chamber allowed the passage of oil inlet tubing

167   and drop outlet tubing (Fig. 2a, Side view). The ports were sealed with silicone sealant (DAP Kwik

168   Seal Plus). A viewport was created using a 1.5 mm-thick transparent polycarbonate sheet that was

169   affixed and sealed to a fabricated opening in the pressure chamber lid, allowing device operation

170   to be monitored or recorded (Fig. 2a, Top view). A strip of white LEDs (Ledmo SMD 2835) was

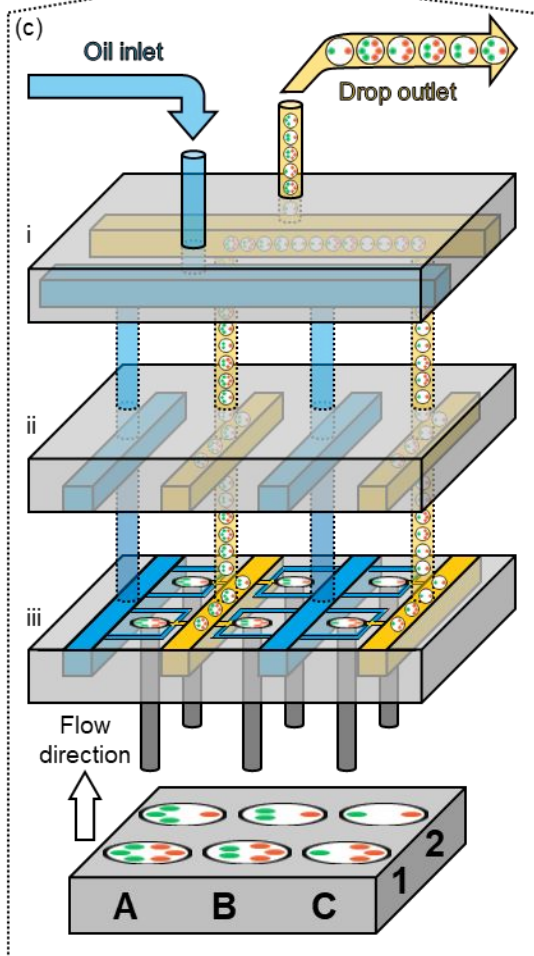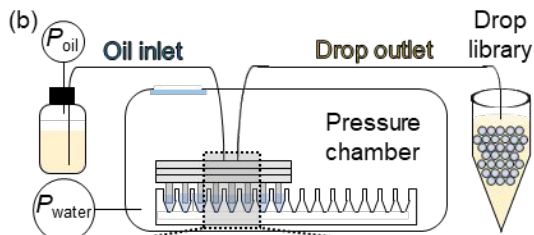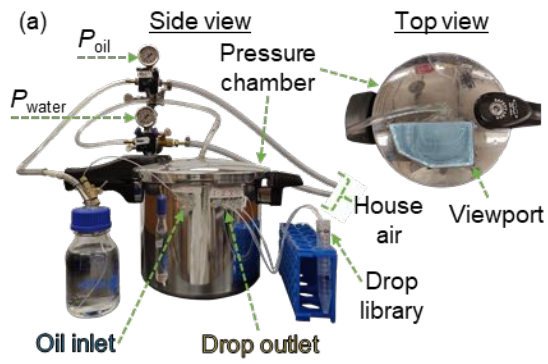171   mounted to the inside of the chamber to provide illumination.

172

173   **Drop Encapsulation**

174   Barcoded samples were pipetted into individual wells of a 384-well microtiter plate and

175   then placed into the pressure chamber apparatus. The PIPE chip was connected to the oil inlet and

176   drop outlet tubing and positioned with the inlet capillaries extending into the wells of the microtiter

177   plate containing barcoded samples (Fig. 2b). An oil reservoir was pressurized by house air and was

178   regulated at pressure P_{oil} to control the oil flowrate. The oil reservoir contained Novec 7500

179   fluorinated oil (3M) with 1.5% w/w of a Krytox-PEG surfactant that was synthesized in-house

180   following a previously published protocol incorporating Jeffamine ED900 (Huntsman) as the

181   hydrophilic portion of the PTFE-PEG-PTFE triblock perfluorosurfactant.[28] The water flowrate

182   was controlled by a second regulator which adjusted P_{water} within the chamber, driving barcoded

183   samples from each microtiter plate well into the PIPE chip to be encapsulated into drops. Barcoded

184   drops were passed through the wall of the pressure chamber before reaching a collection tube to

185   form a library of drops, each indexed to a unique sample well. Drop collection continued for 2-3

186   min, or until air bubbles were observed in the outlet tubing, indicating sample wells were empty.

187   A detailed schematic summarizes barcoded drop encapsulation within the PIPE chip where

188   barcoding is represented by a unique combination of green and red fluorescent microbead

189   concentrations in each well (Fig. 2c). The encapsulation process is the same when quantum dots

190   are used. Pressurization of the chamber pushes the fluid from these wells into the bottom PIPE

191   chip layer (Fig. 2c, iii) where drops are formed at individual drop makers. The drops are then

192   collected in shared drop outlet channels formed from the union of channels in the middle and

193   bottom layer (Fig. 2c, ii and iii, yellow). These shared channels are connected to a perpendicular

194   collection channel on the top layer (Fig. 2c, i) through via holes where drops subsequently flow

195   and are collected in a common drop outlet. The flow of oil is the reverse of the flow of drops; a

196   common oil inlet is distributed in the top layer (Fig. 2c, i) to perpendicular channels (Fig. 2c, ii

197   and iii, blue) through via holes until oil reaches the drop makers (Fig. 2c, iii).

(a)

Side view   Top view

P_{oil}
P_{water}
Pressure chamber
House air
Viewport
Drop library
Oil inlet   Drop outlet

(b)
P_{oil}
Oil inlet   Drop outlet   Drop library
Pressure chamber
P_{water}

(c)
Oil inlet
Drop outlet
i
ii
iii
Flow direction
A   B   C
1   2

198
199

200 **Fig. 2** PIPE chip operation and barcoded drop library production. (a) Side view and top view
201 profiles of the PIPE chip apparatus and components. (b) PIPE chip operation schematic for the
202 encapsulation of 96 wells from a 384-well microtiter plate. Pressure P_{oil} is applied to an external
203 oil reservoir to provide oil to the device within the pressure chamber while a second pressure P_{water}
204 applied to the chamber pushes fluid from sample wells into the microfluidic device. Barcoded
205 drops travel through tubing past a sealed opening in the wall of the chamber for collection in a
206 drop library. (c) Detailed schematic of the internal channels and flows within the PIPE chip.
207 Samples in wells (indexed A − C and 1 − 2) barcoded with different concentrations of green and
208 red microbeads are encapsulated in layer (iii), collected in large drop channels (yellow) formed
209 from both layers (ii) and (iii) where they are transported to perpendicular drop collection channels
210 in layer (i). The barcoded drops flow out of the device in a shared drop outlet.
211

212 **Drop Size Measurements**

213   To characterize drop formation, the PIPE chip was placed on a petri dish filled with 10 mL

214 of sterile-filtered deionized water (0.2 μm filter) within the pressure chamber and the oil reservoir

215 was filled with 100 mL of Novec 7500 (3M) oil with surfactant[28] added at 1.5% w/w. Drops were

216 collected across a range of water P_{water} and oil P_{oil} inlet pressure combinations (2-3, 2-6, 2-12, 4-

217 3, 6-3, 6-6, 6-12, 8-9, and 8-12 psig, where combinations are denoted as P_{water} - P_{oil}).

218 Approximately 10 μL of drops were placed on an 8-well Teflon printed slide (Electron Microscopy

219 Sciences, Cat. #63422-06) and imaged under an inverted brightfield microscope (Nikon TE2000).

220 The height of the Teflon well was larger than the drop diameter, as drops regularly formed a bilayer

221 during imaging. A custom image processing script in MATLAB (R2019a) was used to measure

222 drop diameter D_{drop}. To convert the water and oil pressure ratios P_{water}/P_{oil} to volumetric flowrate

223 ratios Q_{water}/Q_{oil}, we measured the volumes V of the oil and water phases after $t = 0.5$-2.5 min of

224 collection for each water and oil pressure condition. In this case, surfactant was not added to the

225 oil phase to allow for drop coalescence and phase separation of oil and water. The volumetric

226 flowrates of each phase were calculated using $Q_i = \frac{V}{t}$ and plotted as Q_{water}/Q_{oil} as a function of

227 P_{water}/P_{oil} (Fig. S1).†

228   Real-time drop formation within the PIPE chip was visualized through the viewport on the

229   pressure cooker using a high-speed camera (Phantom VEO 710L, Vision Research) attached to a

230   tube lens (Model CFM, ISCO-OPTIC) mounted with a 10× objective (NA 0.25). The underside of

231   the PIPE chip was illuminated by a liquid light guide routed through the side of the pressure cooker

232   and attached to an LED light source (SugarCUBE, Ushio America).

233

234   **Fluorescent Microbead Barcodes**

235   Microbead barcodes consisted of unique two-color combinations of approximately 1-μm

236   diameter green and red microbeads (Thermo Scientific Fluoro-Max G0100 ex. 468 / em. 508 nm

237   and R0100 ex. 542 / em. 612 nm). Green and red microbead (stock of 1% solids, approximately

238   2.5×10^7 microbeads/μL) barcode labels were made from five dilutions in water (5.1×10^5, $1.3 \times$

239   10^6, 2.3×10^6, 3.6×10^6, 5.1×10^6 beads/μL). The five dilutions of each microbead color were

240   mixed equally in a combinatorial manner to create a total of 24 barcode labels. The concentration

241   combinations are detailed in Table S1.† Four concentrations of blue microbeads (Thermo

242   Scientific Fluoro-Max B0100 ex. 412 / em. 473 nm, 5.1×10^5, 1.3×10^6, 2.3×10^6, 3.6×10^6

243   microbeads/μL from a stock of 1% solids, approximately 2.5×10^7 microbeads/μL) were randomly

244   spread across 24 microbead-barcoded wells and used as a mock assay signal. For microbead

245   barcoded drop experiments, the oil pressure was set to 3 psig (P_{oil}) and the chamber pressure was

246   set to 2 psig (P_{water}). For the purpose of collecting 24 samples instead of 96, a modification to the

247   PIPE chip was made to allow drop outlet tubing to be directly connected to the drop collection

248   channels of the second layer of the device. This modification provided separate collection from

249   each quadrant of drop makers on the device where each quadrant is comprised of 24 drop makers.

250   A confocal image of the microbead barcoded drops captured in a drop array device[29] is shown in

251   Fig. S2.† The drop library was collected and re-injected into a secondary device for use with a

252   custom drop fluorescence detection system (See ESI *Barcoded Drop Detection* and Fig. S3-4 for

253   details).†[22] The photomultiplier tube (PMT) gain control voltage was set to 0.32 V for microbead

254   barcoded drop detection.

255

256   **Quantum Dot Barcodes**

257   QDs of two colors (Thermo Scientific QD625 and QD705) were used as barcode labels by

258   preparing 12 QD625 (1.15×10^4, 9.68×10^3, 8.00×10^3, 6.48×10^3, 5.12×10^3, 3.92×10^3, $2.88 \times$

259   10^3, 2.00×10^3, 1.28×10^3, 7.20×10^2, 3.20×10^2, 8.00×10^1 pM) and 16 QD705 (1.02×10^4, 9.00

260     $\times 10^3$, 7.84×10^3, 6.76×10^3, 5.76×10^3, 4.84×10^3, 4.00×10^3, 3.24×10^3, 2.56×3, 1.96×10^3,

261   1.44×10^3, 1.00×10^3, 6.40×10^2, 3.60×10^2, 1.60×10^2, 4.00×10^1 pM) dilutions in water. The

262   12 and 16 dilutions were mixed equally in a combinatorial manner to create a total of 192 barcode

263   labels. The concentration combinations are detailed in Table S2.† For drops containing QD

264   barcodes, the oil pressure (P_{oil}) was set to 8 psig while the chamber pressure (P_{water}) was set to 5

265   psig. The PIPE chip was operated twice to create 192 barcodes (96×2). The PMT control voltage

266   was set to 0.45 V for QD barcoded drop detection.

267

268   **Two-channel Fluorescence-activated Drop Sorting**

269   Barcoded drops were injected into a microfluidic drop sorting device[22] at a flowrate of 40

270   μL/h and spacer oil (Novec 7500) without surfactant was injected at a flowrate of 800 μL/h. A

271   sorting electrode driven by a high voltage amplifier (Trek Model 2220-CE) and controlled by a

272   custom LabVIEW program was used to pull drops into a collection channel. The sorting electrode

273   provided a 400 μs pulse of a 25 kHz, 400 V square wave signal when the drop fluorescence signal

274   fell within the threshold values set for a specific barcode (1 – 1.2 V green channel, 0.15 – 0.25 V

275   red channel).

276

Results and Discussion

278   **Drop Formation Characterization**

279   Drops were generated with the PIPE chip under a range of pressures for P_{water} and P_{oil} to

280   identify combinations that produce uniformly-sized drops. We measured D_{drop} and its distribution,

281   as quantified by the coefficient of variation (CV) of D_{drop}, at each pressure combination (Fig. 3a).

282   To observe drop formation across the range of pressures tested, high speed videos of drop

283   formation in the PIPE chip were captured at four extreme water and oil pressure combinations.

284   The four combinations are labeled with corresponding symbols in Fig. 3a-c: high water pressure

285   (■, P_{water} = 6 psig and P_{oil} = 3 psig), low combined pressure (▼, P_{water} = 2 psig and P_{oil} = 3 psig),

286   high combined pressure (▲, P_{water} = 8 psig and P_{oil} = 12 psig) and high oil pressure (♦, P_{water} = 2

287   psig and P_{oil} = 12 psig). Representative images of Videos S1a-d† are presented in Fig. 3b. At high

288   water pressure (■), the greater water volume fraction led to each drop filling the full length of the

289   exit channel and partially extending into the collection channel before drop break-up occurred, a

290   phenomenon not seen with the other three combinations. As drop formation is no longer fully

291   constrained by the flow focusing junction, this extension of the drop into the collection channel

292   may explain the greater polydispersity at this condition, where D_{drop} = 83.9 ± 12.5 μm. At low and

293   high combined pressure conditions (▼, ▲, both at $P_{\text{water}}/P_{\text{oil}}$ = 0.67), drop formation occurred

294   within the exit channel, creating smaller, more uniform drops at the high pressure condition (▲,

295   D_{drop} = 56.2 ± 2.6 μm) than the low pressure condition (▼, D_{drop} = 68.8 ± 5.0 μm). Drop uniformity

296   did not improve with a higher oil volume fraction (♦, CV = 6.0%) when compared to the high

297   combined pressure condition (▲, CV = 4.6%). As the oil volume fraction was increased, drop

298   formation was limited by the 50-μm width of the exit channel, a characteristic of drop formation

299   in the dripping regime.[30, 31] The dripping regime forms highly uniform drops, whose diameters are

300   largely determined by the flowrates and the width of the flow focusing junction.[30, 32, 33] For all the

301   conditions observed, drop break-up occurred at the flow focusing junction which indicates that

302   drop formation was in the dripping regime.[30, 32]

303   The size of drops formed in the dripping regime can be described by a drop scaling law[34],

304   thereby providing a predictive drop formation model for the PIPE chip. A drop scaling law[34]

305   developed for T-junction geometries, and shown to be applicable for flow focusing geometries[35],

306   is fit to the data and defined as:

307    $$\frac{L_{drop}}{w_{channel}} = 1 + \alpha\frac{Q_{water}}{Q_{oil}}$$ (Eq. 1)

308   where L_{drop} is defined as the length of a drop in the channel measured end to end, $w_{channel}$ is the

309   width of the channel (50 μm), Q_{water}/Q_{oil} is the volumetric flowrate ratio, and α is a geometric

310   constant of order 1. To apply the scaling law to our data, pressure ratios are converted to flowrate

311   ratios using a standard curve (Fig. S1)†. We converted L_{drop} from Eq. 1 to drop volume V_{drop} by

312   approximating the shape of the drop as a capsule geometry when drops are elongated within the

313   microfluidic channel (see ESI *PIPE Chip Drop Formation Characterization* for details)†. The best

314   fit of the drop scaling law with V_{drop} plotted as a function of Q_{water}/Q_{oil} is presented as a dotted line

315   in Fig. 3c with $\alpha = 1.70$ and an $R^2 = 0.793$.[34] Drops produced using the PIPE chip can be adjusted

316   by tuning the pressures applied to the oil and aqueous phases, thereby adjusting Q_{water}/Q_{oil} and

317   enabling the generation of drops within a desired range of diameters (≈50-90 μm).

318

319   Drop size distribution improved from a CV of 14.9% to 4.6% as Q_{water}/Q_{oil} was decreased

320   from 2 to 0.17 (Fig. 3c). When $Q_{water}/Q_{oil} < 1$, further reductions in Q_{water}/Q_{oil} have diminishing

321   effects on V_{drop}. In this case, the minimum drop volume (65 pL, correlating to $D_{drop} = 50$ µm) is

322   reached as $Q_{water}/Q_{oil} \rightarrow 0$ due to the 50-µm width of the drop channel ($L_{drop} \approx w_{channel}$ according

323   to Eq. 1). Interestingly, despite the low and high combined pressure conditions having the same

324   pressure ratio and similar measured flowrate ratios ($Q_{water}/Q_{oil} = 0.43$ or 0.53, respectively), they

325   produced drops with different V_{drop}, from 173 ± 37 pL to 94 ± 13 pL. The difference in V_{drop} for

326   similar Q_{water}/Q_{oil} at higher oil flowrates may be attributed to an increased oil phase capillary

327   number Ca which represents the ratio of the viscous drag to surface tension forces acting on a

328   drop. A higher oil phase Ca corresponds to increased drag at the drop formation junction which

329   leads to faster break-up, resulting in a decreased V_{drop}.[30, 35]
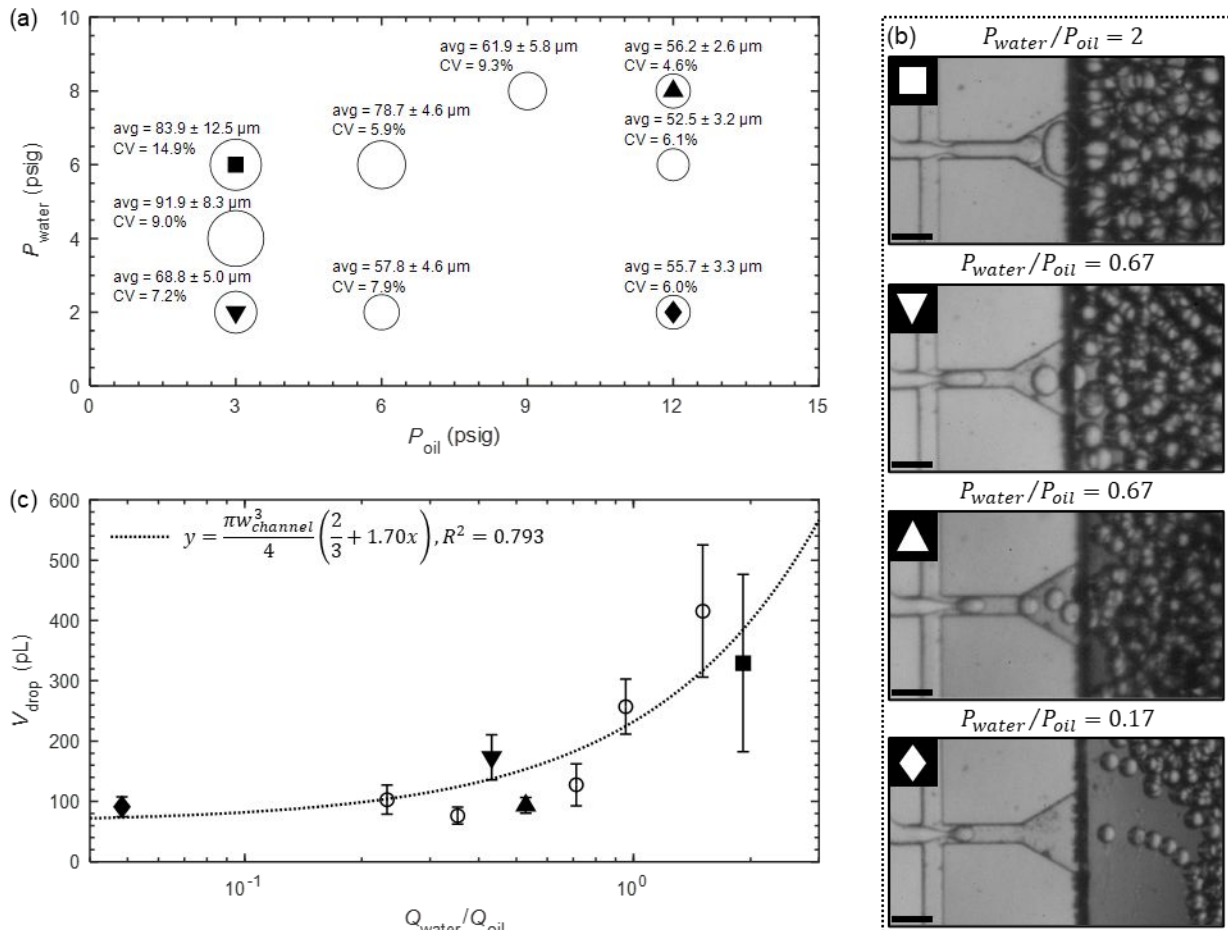
Fig. 3 Characterization of drop sizes produced by the PIPE chip. (a) Drop diameter average, standard deviation, and CV at various water pressures P_{water} and oil pressures P_{oil}. For additional visualization, the relative size of each open circle corresponds to the relative mean drop diameter measured. Solid shapes indicate conditions used for high-speed image capture in (b). (b) High-speed image capture of drop formation, ordered by descending D_{drop}, for high water pressure (■, $P_{water} = 6$ psig and $P_{oil} = 3$ psig, $P_{water}/P_{oil} = 2$), low combined pressure (▼, $P_{water} = 2$ psig and $P_{oil} = 3$ psig, $P_{water}/P_{oil} = 0.67$), high combined pressure (▲, $P_{water} = 8$ and $P_{oil} = 12$ psig, $P_{water}/P_{oil} = 0.67$), and high oil pressure (◆, $P_{water} = 2$ psig and $P_{oil} = 12$ psig, $P_{water}/P_{oil} = 0.17$) conditions. Scale bars = 100 μm. (c) Corresponding drop volumes V_{drop} versus the volumetric flowrate ratio Q_{water}/Q_{oil} (open circles or solid shapes). V_{drop} scales with Q_{water}/Q_{oil} following a drop scaling law (dotted black line).[34] Error bars represent one standard deviation from the mean.

Optimizing Barcode Discrimination in Drop Libraries

345

346   Drop libraries barcoded with fluorescence-based barcodes have recently reached a label

347   count of 1,050 unique combinations with the use of four dye colors.[4] Lanthanide nanophosphors

348   are capable of creating up to 1,023 unique labels with a six-color combination, but have yet to be

349   used in drop libraries.[36] However, using a large number of barcode colors may not be

350   advantageous, as the overlap of emission spectra between the fluorescent reporters can limit the

351   practical number of colors that can be used in an assay.[37, 38] Simply reducing the number of barcode

352   colors to one or two and varying their concentrations can greatly expand the range of usable

353   reporters. Thus, the PIPE chip was used to generate two fluorescently barcoded drop libraries from

354   two-color combinations of either microbeads or QDs. Fluorescent particles were used to prevent

355   diffusion of the barcode labels between drops.[23] The libraries were prepared by mixing different

356   ratios of each color to form distinct combinations on a microtiter plate (see Materials and

357   Methods). The polystyrene microbead drop library was comprised of 24 barcodes made from ratios

358   of green and red fluorescent polystyrene microbeads while the QD drop library was comprised of

359   192 barcodes made from ratios of QDs with peak emissions at 625 and 705 nm. The PIPE chip

360   was used to simultaneously encapsulate all the barcoded contents of the plate in 2 min, creating

361   approximately 3.75×10^5 drops ($D_{drop} = 50$ μm) per barcode. Barcoded drops were reinjected into

362   a microfluidic device for analysis using a laser-induced fluorescence detection system.[22] Drop

363   fluorescence was measured as the drops flowed past a laser at approximately 300 Hz.

364   Contributions from spectral crosstalk and sources of noise limit the number of barcodes

365   that can be identified after library reinjection. The narrow emission spectra of QDs leads to less

366   spectral crosstalk between each barcoding color compared to the microbeads. This can be observed

367   in the raw data of the 24 microbead fluorescence intensities (Fig. 4a) compared to the 192 QD

368 fluorescence intensities (Fig. 4b). Due to the wide emission spectra of the microbeads, the emission

369 of the green microbeads overlaps with the red microbeads. This causes barcodes with high green

370 intensity to appear more red, skewing the data to the upper right (Fig. 4a). The effect of spectral

371 crosstalk also skews the QD data (Fig. 4b), but due to the narrow emission spectra of the QDs, the

372 effect is lower in magnitude compared to the microbeads.

373   We applied a clustering algorithm, Density-Based Spatial Clustering of Applications with

374 Noise (DBSCAN), to identify and separate "clusters" of specific barcoded drops within the

375 libraries.[24] Densely packed data points are assigned to clusters by DBSCAN while outlier data

376 points in low-density regions are marked as noise. When the data are graphed on a linear plot,

377 DBSCAN was able to group 70% of the 1.31×10^4 drops containing microbeads into 24 clusters

378 (Fig. 4a, blue dots) and 30% as noise (Fig. 4a, black dots), with a mean of 399 ± 201 drops per

379 barcode (CV = 50.4%). However, DBSCAN was not able to completely identify clusters in the

380 QD raw data (Fig. 4b, blue dots). Of the clusters identified, DBSCAN grouped 76% of the $1.27 \times$

381 10^5 drops containing QDs with a range of 15 to 6,033 drops per barcode (mean of 508 ± 478 drops

382 and CV = 94.1%). A significant number of clusters were mislabeled as noise (Fig. 4b, upper right

383 black dots) due to the large variability in cluster density.

384   To better understand the variability between barcode clusters, we identify two major

385 sources of variation in our data, both a direct consequence of particle size: *Poisson loading* for

386 microbeads and *shot noise* for QDs. The loading of approximately 1-μm diameter fluorescent

387 microbeads into drops is dependent upon Poisson statistics. The fluorescence signal obtained from

388 drops containing microbeads follows a Poisson distribution due to the discrete nature of particle

389 loading in drops.[22] The Poisson distribution is described by the equation:

390      $$P = \frac{\lambda^k e^{-\lambda}}{k!}$$ (Eq. 2)

391   where P is the probability distribution of drops that contain k number of particles with a mean

392   number of particles per drop λ. Variability inherent to Poisson loading[22] is represented by the

393   standard deviation of the number of particles in drops $\sigma_{particle} = \lambda^{1/2}$. We plot a representative subset

394   of five red microbead barcodes (Fig. 4c, black dots) corresponding to the clusters in Fig. 4a (dashed

395   red boxes). The subset is compared to estimated Poisson distributions centered around the

396   microbead loading concentrations $\lambda = 33, 83, 149, 232$, and 333 beads/drop where λ is converted

397   to voltage using an experimentally verified linear standard curve relating PMT output voltage to

398   microbead concentration (beads/drop, λ) (Fig. S7a).† The probability of microbead distributions

399   (Fig. 4c, dashed red line) closely tracks the PMT voltage measurements of the red microbead data

400   (Fig. 4c, black dots) with $R^2 = 0.931$.

401   When the particle size is far below the objective resolution, for example in the case of QDs

402   that are approximately 10 nm in diameter, the variability in drop fluorescence is no longer a

403   function of the number of discrete particles in drops, but is instead governed by the shot noise of

404   the PMT. Shot noise is inherent to counting photons with a PMT and contributes to the

405   fluorescence signal in low light environments such as high-speed detection of drop fluorescence.[39,]

406   [40] We plot the signal distributions of a 12 QD625 barcode subset of the QD barcoded library (Fig.

407   4d, black dots) corresponding to the clusters outlined in Fig 4b (dashed green boxes). The Schottky

408   equation approximates shot noise[40, 41] in which the standard deviation of the PMT voltage σ_{shot} is

409   proportional to the square root of the mean PMT voltage $\mu_{intensity}$ (see ESI *Schottky Equation* for

410   details).† The subset of QD data is compared to normal distributions defined by $\mu_{intensity}$ and σ_{shot}

411   for each QD barcode. The value of $\mu_{intensity}$ is determined by an experimentally verified linear

412   standard curve relating PMT output voltage to QD concentration (nM) (Fig. S7b, Eq. S1)†. The

413   probability of QD distributions (Fig 4d, dashed green line) closely tracks the PMT voltage

414   measurements of the QD625 data (Fig 4d, black dots) with $R^2 = 0.852$.

415   To demonstrate that the remainder of the experimental microbead and QD barcode data

416   follow either Poisson loading or shot noise, barcode clusters are manually grouped and compared

417   to theoretical estimates of $\sigma_{particle}$ (Fig. 4c-d, inset, dashed red line) and σ_{shot} (Fig. 4c-d, inset, dotted

418   green line, see ESI *Calculation of Noise* for details).† Drop library fluorescence data are manually

419   grouped by drawing lines around each cluster by eye (Fig. S8)† to isolate individual barcode signal

420   populations for each PMT channel. The mean $\mu_{barcode}$ and standard deviation $\sigma_{barcode}$ of the

421   manually-segmented 24 microbead and 192 QD signal distributions are calculated for each PMT

422   channel, yielding 48 and 384 values of $\mu_{barcode}$ and $\sigma_{barcode}$. The $\sigma_{barcode}$ is plotted against $\mu_{barcode}^{1/2}$ for

423   each grouped microbead and QD barcode population (Fig. 4c-d, inset, black dots). The

424   experimental $\sigma_{barcode}$ of the microbeads closely follows the theoretical estimate of particle loading

425   noise $\sigma_{particle}$ (Fig. 4c, inset, dashed red line). The $\sigma_{barcode}$ is approximately an order of magnitude

426   greater than the theoretical estimate of shot noise σ_{shot} (Fig. 4c, inset, dotted green line). Therefore,

427   across all drops, the discrimination of microbead barcode signals is limited by particle loading

428   noise as the dominant source of variation. By contrast, the experimental $\sigma_{barcode}$ of the QDs closely

429   follows the theoretical estimate of shot noise σ_{shot} (Fig. 4d, inset, dotted green line) and is

430   approximately an order of magnitude greater than the estimate of particle loading noise $\sigma_{particle}$

431   (Fig. 4d, inset, dashed red line), indicating the data is shot noise-limited. The narrow emission

432   spectrum of the QDs results in a 1-2 log decrease of σ_{shot} compared to $\sigma_{particle}$. This enables an 8×

433   increase in unique barcode concentrations obtained with QDs compared to microbeads (192 versus

434   24).

435   As signal variation depends upon Poisson loading for microbeads ($\sigma_{particle} \propto \lambda^{1/2}$) and shot

436   noise for QDs ($\sigma_{shot} \propto \mu^{1/2}$), scaling the intensity data for both barcode libraries by a square root

437   function linearizes the noise. This scaling spaces each barcode grouping as shown in Fig. 4e-f (Fig.

438   S5-6)†. When DBSCAN is applied to the scaled data, the increased spacing allows for improved

439   clustering of each barcode compared to the unscaled raw data (Fig. 4a-b). Of the 1.31×10^4

440   microbead barcoded drops detected, DBSCAN was able to group 74.8% of the data into 24 clusters

441   (Fig. 4e, blue dots) and identify 25.2% as noise (Fig. 4e, black dots) with a mean of 408 ± 62 drops

442   per barcode (CV = 15.2%). The CV of clustered square root scaled data is greatly reduced from

443   50.4% with the linearly scaled data (Fig. 4a) to 15.2% with the square root scaled data (Fig. 4e).

444   Additionally, a square root scaling of the QD data allows DBSCAN to correctly identify 188 out

445   of the 192 of barcoded drop populations where the missing four populations are due to two clogged

446   drop makers on the PIPE chip and are indicated by the yellow ovals (Fig. 4f). Of the 1.27×10^5

447   QD barcoded drops detected, DBSCAN was able to group 85.4% of data into 188 clusters (Fig.

448   4f, blue dots) and identify 14.6% as noise (Fig. 4f, black dots) with a mean barcode cluster size of

449   576 ± 88 drops (CV = 15.3%). Once again, the CV is greatly reduced from 94.1% with the linearly-

450   scaled quantum dot data to 15.5% with the square root-scaled data.

451   Previous examples of drop libraries using one or two fluorescence dye colors have realized

452   up to eight[10] or sixteen[11] unique labels. Using the PIPE chip, we achieved a total of 188 discrete

453   barcodes with two-color combinations of QDs. To our knowledge, this is the largest two-color

454   fluorescent barcode combination in drops to date. Additionally, the effect of particle size on signal

455   noise can be described empirically and used for future experiments to inform the selection of

456   barcode concentrations.

457

458
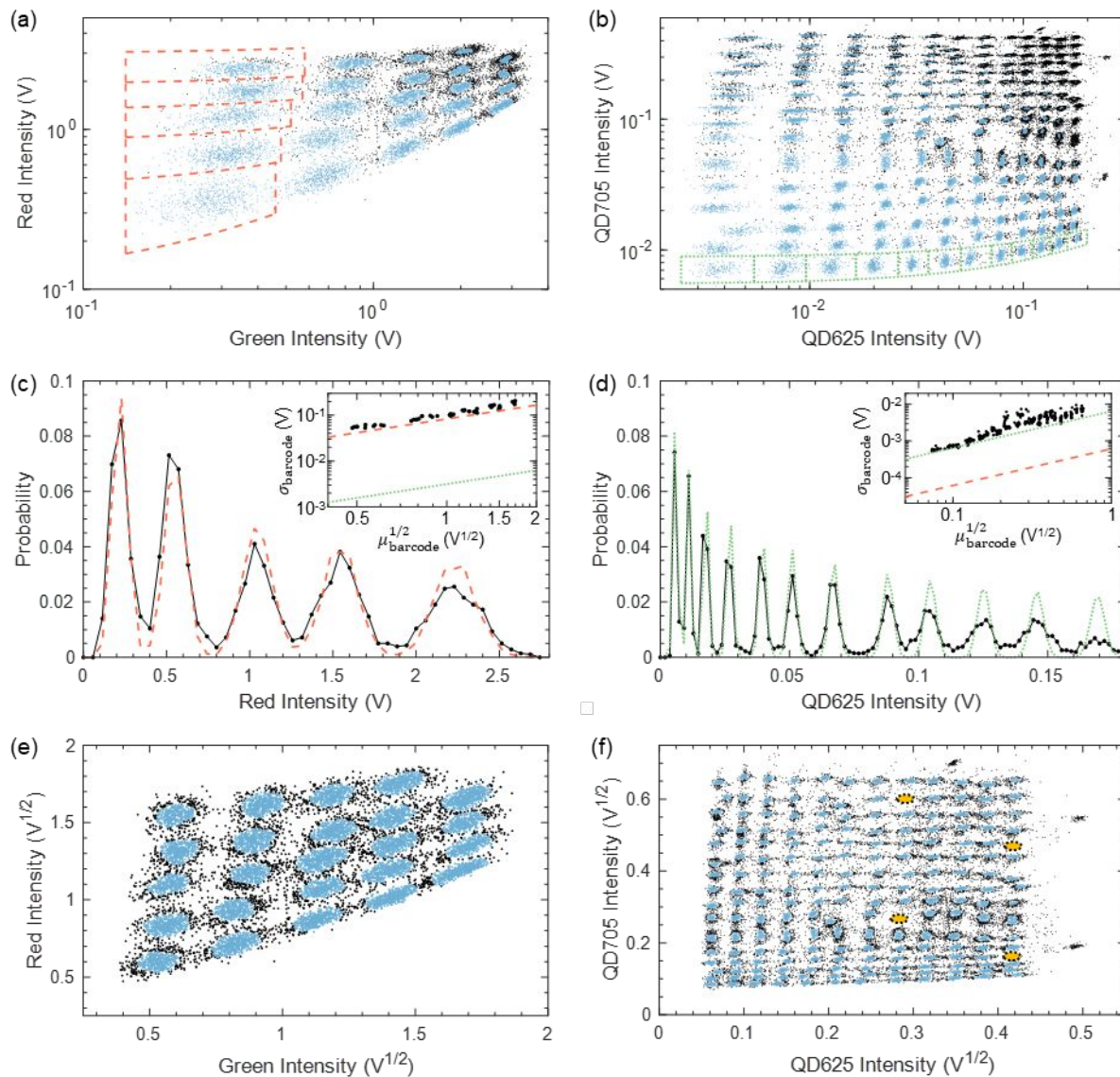
Fig. 4 Analysis of microbead and QD barcoded drop libraries. Scatter plots of (a) microbead and (b) QD fluorescence intensity in the drop library. Clusters identified by DBSCAN are indicated in blue while noise is in black. Probability distributions of (c) five red microbead barcoded drop populations (black dots) plotted against the particle loading noise estimate (dashed red line, $R^2 = 0.931$) and (d) twelve QD625 barcoded drop populations (black dots) plotted against the shot noise estimate (dotted green line, $R^2 = 0.852$). Solid black lines guide the eye for the measured microbead and QD625 data. Inset (c-d): standard deviations of each barcode σ_{barcode} (black dots) plotted against $\mu_{\text{barcode}}^{1/2}$ with estimates for σ_{particle} (dashed red line) and σ_{shot} (dotted green line). Scatter plots of (e) microbead and (f) QD drop library data scaled by $V^{1/2}$. Clusters identified by DBSCAN are indicated in blue while noise is in black. Missing clusters in (f) are due to two clogged channels in the PIPE chip and are indicated by dotted yellow ovals.

470

Sample Isolation Using Fluorescence-activated Drop Sorting

471

472   To demonstrate the utility of the PIPE chip, fluorescence-activated drop sorting[21, 22] was

473   performed to isolate drops of a single barcode population within a drop library of 24 green and red

474   microbead combinations spiked with four concentrations of blue microbeads. We verify that the

475   desired green and red barcode combination was isolated by detecting a single concentration of the

476   blue microbeads. A barcode from the drop library was chosen by designating a box with upper and

477   lower fluorescence intensity bounds in the green and red fluorescence channels (Fig. 5a, red box).

478   Recovery of the desired barcode population is confirmed by performing flow-based fluorescence

479   detection on the sorted drops, yielding an isolated barcode cluster with intensity bounds close to

480   those originally chosen in the green and red channels (Fig. 5b). However, there is an observed shift

481   in fluorescence signal distribution from pre- to post-sort (Fig. 5a-b) where the post-sort data has

482   shifted by ≈ 0.2 V along the *x*-axis. This shift is likely caused by run-to-run variation arising from

483   the positioning of the laser in the device channel. Post-processing of the sorted drop data using

484   DBSCAN provides a clear distinction between the target barcode population (Fig. 5b, red dots)

485   and the outlier data points (Fig. 5b, open black circles). The outlier points comprise 7.5% of the

486   drop data.

487   The four populations of blue microbead-barcoded drops were detected in the pre-sort drop

488   library (Fig. 5c). Fluorescence detection of the sorted drops yielded a single blue microbead

489   population with few outliers (Fig. 5d), matching the highest blue microbead concentration (Fig.

490   5c, arrow). DBSCAN clustering of corresponding green and red fluorescence identifies these

491   outliers (Fig. 5d, black bars) and the target sorted population (Fig. 5d, red bars). The outliers

492   comprise 5.9% of the sorted population, in close agreement with the data corresponding to the

493   green and red barcoded drops (Fig. 5b). These results demonstrate the ability to isolate a single

494   barcoded population from a drop library created using the PIPE chip, critical for performing

495   downstream assays.
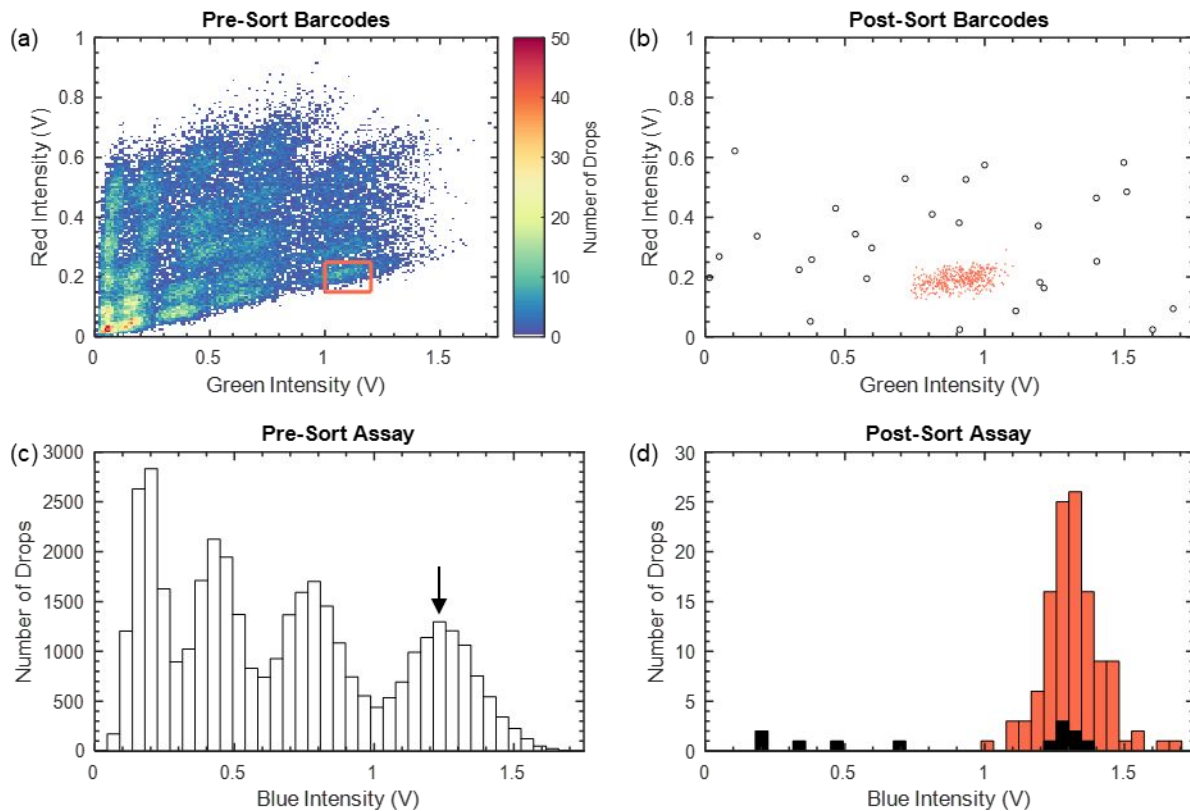
496

497   **Fig. 5** Fluorescence-activated drop sorting of a microbead-barcoded drop library. (a) Fluorescence
498   intensity of barcoded drops before sorting. The sorted region is indicated by the red box. (b)
499   Fluorescence intensity of barcoded drops after sorting. DBSCAN is used to separate the outlier
500   data points (open black circles) from the target barcode population (red dots). (c) Distribution of
501   four concentrations of blue microbead drops within the drop library. (d) Distribution of blue
502   microbeads in the sorted barcoded drop population shows a single peak corresponding to the
503   largest concentration of blue microbeads. DBSCAN is used to separate the outliers (black bars)
504   from the target sorted population (red bars).

505

506

507

508

Conclusions

Here we have demonstrated tunable parallel production of 50 to 90 μm diameter drops containing upwards of 96 different loading conditions from a microtiter plate, improving upon the previously published limit of 24.[20] By scaling the signal noise with the square root of the intensity, barcoded drop libraries comprised of 24 microbead barcodes or 192 QD barcodes are distinguishable using DBSCAN.[24] Barcode number is ultimately limited by microbead or QD signal resolution. As a function of size, signal resolution between larger microbeads was limited by Poisson loading noise while the signals from the smaller QD barcodes were limited by shot noise. This empirical relationship found between signal noise and barcode concentration can be used to quickly prototype barcode label concentrations for future experiments. Utilizing two-color combinations of QDs, we achieved a total of 188 discrete barcodes, the largest two-color fluorescence barcode combination in drops published to date. The addition of a third QD color, offering up to 16 unique concentrations, would enable QDs to easily index multiple 384-well microtiter plates using as many as 3,072 unique barcodes ($12 \times 16 \times 16$), far surpassing what has been achieved with four color combinations (1,050 labels).[4] Furthermore, we have shown that barcoded populations can be selectively sorted with minimal error (5.9-7.5%), demonstrating that downstream analysis of a specific sample population is possible. By reducing sample encapsulation time and enabling rapid, parallel generation of a barcoded library directly from a microtiter plate, we envision that the PIPE chip will further advance multiplexed assaying in applications including combinatorial drug screening,[3, 10] DNA microarray analysis,[11] or enzyme activity screening.[12]

Conflicts of Interest

There are no conflicts to declare.

Acknowledgments

Author Contributions

G.K.Z., R.A.S., A.R.A., D.A.W. and C.B.C. designed research; G.K.Z., R.A.S, C.W.H., and R.A. performed research; G.K.Z. and R.A.S. analyzed data; and G.K.Z., R.A.S., C.W.H., D.A.B., and C.B.C. wrote the manuscript.

References

554   1.   J. J. Agresti, E. Antipov, A. R. Abate, K. Ahn, A. C. Rowat, J.-C. Baret, M. Marquez, A.
555   M. Klibanov, A. D. Griffiths and D. A. Weitz, *Proceedings of the National Academy of*
556   *Sciences*, 2010, **107**, 4004-4009.

557   2.   M. T. Guo, A. Rotem, J. A. Heyman and D. A. Weitz, *Lab on a Chip*, 2012, **12**, 2146-
558   2155.

559   3.   A. Kulesa, J. Kehe, J. E. Hurtado, P. Tawde and P. C. Blainey, *Proceedings of the*
560   *National Academy of Sciences*, 2018, **115**, 6685-6690.

561   4.   C. M. Ackerman, C. Myhrvold, S. G. Thakku, C. A. Freije, H. C. Metsky, D. K. Yang, H.
562   Y. Simon, C. K. Boehm, T.-S. F. Kosoko-Thoroddsen and J. J. N. Kehe, *Nature*, 2020, 1-
563   6.

564   5.   O. Scheler, K. Makuch, P. R. Debski, M. Horka, A. Ruszczak, N. Pacocha, K. Sozański,
565   O.-P. Smolander, W. Postek and P. J. S. r. Garstecki, *Scientific Reports (Nature Publisher*
566   *Group)*, 2020, **10**, 1-8.

567   6.   A. M. Klein, L. Mazutis, I. Akartuna, N. Tallapragada, A. Veres, V. Li, L. Peshkin, D. A.
568   Weitz and M. W. J. C. Kirschner, *Cell*, 2015, **161**, 1187-1201.

569   7.   A. Rotem, O. Ram, N. Shoresh, R. A. Sperling, A. Goren, D. A. Weitz and B. E.
570   Bernstein, *Nature biotechnology*, 2015, **33**, 1165-1172.

571   8.   A. Rotem, O. Ram, N. Shoresh, R. A. Sperling, M. Schnall-Levin, H. Zhang, A. Basu, B.
572   E. Bernstein and D. A. Weitz, *PloS one*, 2015, **10**, e0116328.

573   9.   E. Z. Macosko, A. Basu, R. Satija, J. Nemesh, K. Shekhar, M. Goldman, I. Tirosh, A. R.
574   Bialas, N. Kamitaki and E. M. Martersteck, *Cell*, 2015, **161**, 1202-1214.

575   10.   E. Brouzes, M. Medkova, N. Savenelli, D. Marran, M. Twardowski, J. B. Hutchison, J.
576   M. Rothberg, D. R. Link, N. Perrimon and M. L. Samuels, *Proceedings of the National*
577   *Academy of Sciences*, 2009, **106**, 14195-14200.

578   11.   A. R. Abate, T. Hung, R. A. Sperling, P. Mary, A. Rotem, J. J. Agresti, M. A. Weiner and
579   D. A. Weitz, *Lab on a Chip*, 2013, **13**, 4864-4869.

580   12.   C. H. Chen, M. A. Miller, A. Sarkar, M. T. Beste, K. B. Isaacson, D. A. Lauffenburger,
581   L. G. Griffith and J. Han, *Journal of the American Chemical Society*, 2013, **135**, 1645-
582   1648.

583   13.   J. Kehe, A. Kulesa, A. Ortiz, C. M. Ackerman, S. G. Thakku, D. Sellers, S. Kuehn, J.
584   Gore, J. Friedman and P. C. Blainey, *Proceedings of the National Academy of Sciences*,
585   2019, **116**, 12804-12809.

586   14.   O. J. Miller, A. El Harrak, T. Mangeat, J. C. Baret, L. Frenz, B. El Debs, E. Mayot, M. L.
587   Samuels, E. K. Rooney, P. Dieu, M. Galvan, D. R. Link and A. D. Griffiths, *Proceedings*
588   *of the National Academy of Sciences*, 2012, **109**, 378-383.

589   15.   T. S. Kaminski, S. Jakiela, M. A. Czekalska, W. Postek and P. Garstecki, *Lab on a Chip*,
590   2012, **12**, 3995-4002.

591   16.   T. D. Rane, H. C. Zec and T.-H. Wang, *Journal of laboratory automation*, 2012, **17**, 370-
592   377.

593   17.   J. Clausell-Tormos, A. D. Griffiths and C. A. Merten, *Lab on a Chip*, 2010, **10**, 1302-
594   1307.

595   18.   M.-P. N. Bui, C. A. Li, K. N. Han, J. Choo, E. K. Lee and G. H. Seong, *Analytical*
596   *chemistry*, 2011, **83**, 1603-1608.

597   19.   J. Lim, O. Caen, J. Vrignon, M. Konrad, V. Taly and J.-C. Baret, *Biomicrofluidics*, 2015,
598   **9**, 034101.

599   20.   L. A. Bawazer, C. S. McNally, C. J. Empson, W. J. Marchant, T. P. Comyn, X. Niu, S.
600   Cho, M. J. McPherson, B. P. Binks, A. deMello and F. C. Meldrum, *Science Advances*,
601   2016, **2**.

602   21.   J. C. Baret, O. J. Miller, V. Taly, M. Ryckelynck, A. El-Harrak, L. Frenz, C. Rick, M. L.
603   Samuels, J. B. Hutchison, J. J. Agresti, D. R. Link, D. A. Weitz and A. D. Griffiths, *Lab*
604   *on a Chip*, 2009, **9**, 1850-1858.

605   22.   L. Mazutis, J. Gilbert, W. L. Ung, D. A. Weitz, A. D. Griffiths and J. A. Heyman, *Nature*
606   *protocols*, 2013, **8**, 870-891.

607   23.   P. Gruner, B. Riechers, B. Semin, J. Lim, A. Johnston, K. Short and J.-C. Baret, *Nature*
608   *communications*, 2016, **7**, 1-9.

609   24.   M. Ester, H.-P. Kriegel, J. Sander and X. Xu, Portland, OR, 1996.

610   25.   S. W. Lim, T. M. Tran and A. R. Abate, *PloS one*, 2015, **10**, e0113549.

611   26.   H. Zhang, S. K. Cockrell, A. O. Kolawole, A. Rotem, A. W. Serohijos, C. B. Chang, Y.
612   Tao, T. S. Mehoke, Y. Han and J. S. Lin, *Journal of virology*, 2015, **89**, 7722-7734.

613   27.   Y. Tao, A. Rotem, H. Zhang, S. K. Cockrell, S. A. Koehler, C. B. Chang, L. W. Ung, P.
614   G. Cantalupo, Y. Ren and J. S. J. C. Lin, *ChemBioChem*, 2015, **16**, 2167-2171.

615   28.   C. Holtze, A. C. Rowat, J. J. Agresti, J. B. Hutchison, F. E. Angile, C. H. Schmitz, S.
616   Koster, H. Duan, K. J. Humphry, R. A. Scanga, J. S. Johnson, D. Pisignano and D. A.
617   Weitz, *Lab Chip*, 2008, **8**, 1632-1639.

618   29.   C. H. Schmitz, A. C. Rowat, S. Köster and D. A. Weitz, *Lab on a Chip*, 2009, **9**, 44-49.

619   30.   T. Cubaud and T. G. Mason, *Physics of Fluids*, 2008, **20**, 053302.

620   31.   J. D. Tice, A. D. Lyon and R. F. Ismagilov, *Analytica chimica acta*, 2004, **507**, 73-77.

621   32.   D. Funfschilling, H. Debas, H.-Z. Li and T. Mason, *Physical Review E*, 2009, **80**,
622   015301.

623   33.   P. Garstecki, H. A. Stone and G. M. Whitesides, *Physical review letters*, 2005, **94**,
624   164501.

625   34.   P. Garstecki, M. J. Fuerstman, H. A. Stone and G. M. Whitesides, *Lab on a Chip*, 2006,
626   **6**, 437-446.

627   35.   A. Abate, A. Poitzsch, Y. Hwang, J. Lee, J. Czerwinska and D. Weitz, *Physical Review
628   E*, 2009, **80**, 026310.

629   36.   H. Q. Nguyen, B. C. Baxter, K. Brower, C. A. Diaz-Botia, J. L. DeRisi, P. M. Fordyce
630   and K. S. Thorn, *Advanced optical materials*, 2017, **5**, 1600548.

631   37.   M. Han, X. Gao, J. Z. Su and S. Nie, *Nature biotechnology*, 2001, **19**, 631.

632   38.   H. Lee, J. Kim, H. Kim, J. Kim and S. Kwon, *Nature materials*, 2010, **9**, 745-749.

633   39.   A. Huebner, M. Srisa-Art, D. Holt, C. Abell, F. Hollfelder, A. Demello and J. J. C. c.
634   Edel, *Chemical communications*, 2007, 1218-1220.

635   40.   R. L. McClain and J. C. Wright, *Journal of Chemical Education*, 2014, **91**, 1455-1457.

636   41.   W. Schottky, *Annalen der Physik*, 1918, **362**, 541-567.

637
638